



# Visual light-driven valorization of biomass-based 5-hydroxymethylfurfural over ZnS/ZnIn<sub>2</sub>S<sub>4</sub> heterostructures as hollow nanoreactors

Yuxin Zhang<sup>a</sup>, Ming Zhang<sup>a</sup>, Zhihao Yu<sup>a,\*</sup>, Runyu Liu<sup>a</sup>, Yiming Li<sup>a</sup>, Jian Xiong<sup>b</sup>, Yina Qiao<sup>c</sup>, Rui Zhang<sup>d</sup>, Xuebin Lu<sup>a,b,\*</sup>

<sup>a</sup> School of Environmental Science and Engineering, Tianjin University, Tianjin, 300350, PR China

<sup>b</sup> School of Ecology and Environment, Tibet University, Lhasa 850000, PR China

<sup>c</sup> School of Environment and Safety Engineering, North University of China, Taiyuan 030051, PR China

<sup>d</sup> School of Environmental and Municipal Engineering, Tianjin Chengjian University, Tianjin 300384, PR China

## ARTICLE INFO

### Keywords:

Biomass valorization  
5-hydroxymethylfurfural  
S-scheme heterostructures  
Hollow nanoreactor

## ABSTRACT

Hollow heterostructured nanoreactors have been used as one of the top choices for photocatalytic valorization conversion of biomass platform molecules due to their superior light-absorbing ability, high efficiency of photogenerated carrier separation and migration, ability to add a large number of reaction sites to the reaction, and good stability. In this paper, an ortho-dodecahedral hollow core-shell ZnS/ZnIn<sub>2</sub>S<sub>4</sub> heterostructured catalyst was developed for value-added biomass conversion. The catalyst photocatalytically oxidized 5-hydroxymethylfurfural to 2,5-dicarbonylfuran in 70.9 % yield under mild oxygen and visible light conditions without the addition of other auxiliary substances. Based on the characterization results and theoretical derivations, S-scheme heterojunctions with high photogenerated carrier separation-migration efficiencies are proposed. The main reactive radicals for the photocatalytic conversion of 5-hydroxymethylfurfural to 2,5-dicarbonylfuran were identified as hole radicals and superoxide radicals by electron paramagnetic resonance spectroscopy and trap experiments, and the catalysts had a good universality of oxidising biomass.

## 1. Introduction

Towards sustainable development, it is crucial to explore and develop renewable sources of carbon. In this regard, biomass maintains a strong momentum due to its circular economy feature. Consumers consuming it instead of high-carbon energy sources will not change the current carbon balance of the ecosystem and is in line with the strategic direction of green energy [1–3]. 5-Hydroxymethylfurfural (HMF) is a renewable C6 biomass-derived platform molecular chemical that allows for the selective oxidation of various high-value-added derivatives [4]. As one of the crucial derivatives, 2,5-diformylfuran (DFF) has been widely used as a pharmaceutical intermediate, an organic conductor and a monomer for functional polymers. The preparation of DFF using HMF is one of the important routes in the phase of value-added molecular conversion of furfural biomass platforms, but the current conventional preparation methods, such as thermal and electrocatalytic, are prone to induce safety and environmental hazards. To comply with the green chemistry and sustainability perspectives[5], it is of utmost importance to develop an effective and highly selective conversion of HMF to DFF

under mild conditions, and photocatalytic technologies driven by light and airborne oxygen are of great interest due to their high environmental sustainability[6–9].

Metal sulfides are semiconductor photocatalysts featuring highly dynamic properties. In contrast to metal oxides, the hole carriers of metal sulfides usually have a smaller effective mass than those of metal oxides, which indicates higher hole mobility and better charge transfer in metal sulfides[10]. In Furthermore, the tunable surface properties, excellent solar spectral response and high photocatalytic activity of sulfide photocatalysts have brought much attention to them [11]. The coupling of metal sulfides to build rational heterojunction structures can accelerate the separation and transfer of photoexcited charges efficiently by utilizing the potential gradient between the heterogeneous interfaces [12]. Multicomponent heterostructures consisting of rich interfaces can integrate different building blocks into a single entity and generate extraordinary functions through synergistic interactions [13], such as light stabilization and harvesting capabilities. These advantages can lead to stronger photocatalytic performance of heterogeneous structures. In addition to the control of heterogeneous structure and chemical

\* Correspondence to: School of Environmental Science and Engineering, Tianjin University, Tianjin, 30000, P. R. China.

E-mail addresses: [zhihaoyupublic@tju.edu.cn](mailto:zhihaoyupublic@tju.edu.cn) (Z. Yu), [xbltju@tju.edu.cn](mailto:xbltju@tju.edu.cn) (X. Lu).

<https://doi.org/10.1016/j.apcatb.2024.123914>

Received 10 January 2024; Received in revised form 27 February 2024; Accepted 3 March 2024

Available online 5 March 2024

0926-3373/© 2024 Elsevier B.V. All rights reserved.

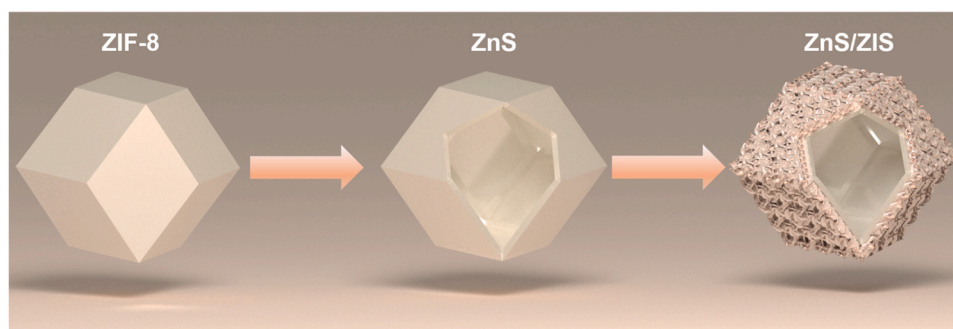


Fig. 1. ZnS/ZIS preparation process.

composition, the realization of efficient photocatalytic reaction also depends largely on the meticulous design of the catalyst structure.

Morphology-controlled nanocatalysts can enhance the intrinsic catalytic activity of various metal nanoparticles [14], and the same strategy can be expanded to boost the catalytic performance of metal sulfides. Recently, hollow nanoreactors with peculiar structural properties and favorable performance have been intensively investigated as photocatalysts for solar energy conversion [15]. Hollow nanoreactors not only shorten the vertical diffusion distance to accelerate the separation of photogenerated charges [16] but also provide a large surface area for the deposition of other materials and an abundance of exposed active sites to facilitate redox reactions [17]. Hollow nanoreactors, especially polyhedral cages, can enhance light absorption by internal multiple light scattering/reflection [18,19].

Herein, a heterostructure with in situ loading of  $\text{ZnIn}_2\text{S}_4$  (ZIS) nanosheets on the surface of hollow ZnS shells was successfully developed for photocatalytic HMF to DFF by rational design in this paper. The catalytic DFF yield was increased to 2.5 times after loading ZnS compared to pure ZIS. It is indicated that the enhancement of photocatalytic performance owed to the unique hollow nanoreactor exposing more active sites, cutting off the recombination paths of holes and electrons, and the constructed heterojunctions provided lower photo-generated carrier recombination rates. This work offers new thoughts in the field of photocatalytic biomass valorization and demonstrates the advancement of constructing hollow heterojunction materials.

## 2. Experimental work

### 2.1. Preparation of hollow and non-hollow ZnS

Ortho-dodecahedral ZnS hollow shells were prepared with ZIF-8 as a precursor. 4 mmol of zinc nitrate hexahydrate and 8 mmol of 2-methylimidazole were dissolved in 100 mL of methanol, respectively. Then the above two solutions were mixed under magnetic stirring for 3 min, and after the mixing was completed, they were aged and incubated at room temperature for 12 h. The white sediments obtained were washed with ethanol and later dried under vacuum at 50 °C for 12 h to obtain the ZIF-8 dodecahedral cage. The sulfur source was added afterward for etching. The resulting 20 mg of ZIF-8 and 400 mg of thioacetamide (TAA) were dispersed in 50 mL of ethanol and subjected to a classical hydrothermal reaction in a Teflon-lined 100 mL autoclave (Anhui Kemi Machinery Technology Co., Ltd.) at 120 °C for 30 min. After that, it was washed with ethanol and dried under vacuum conditions at 50 °C for 12 h.

Non-hollow ZnS was synthesized directly by hydrothermal method without using precursors. 1.19 g of zinc nitrate hexahydrate and 300 mg of TAA were added to 50 mL of ethanol in a reactor and hydrothermally heated for 30 min at 120 °C. The alcohol was washed and then vacuum dried at 50 °C for 12 h.

### 2.2. ZnS/ZIS heterostructures preparation

8 mL glycerol was added to 32 mL aqueous HCl solution (pH = 2.5), and then a certain amount of ZnS (100 mg, 75 mg, 50 mg, 25 mg) was added and stirred for 30 min. 272 mg  $\text{ZnCl}_2$ , 586 mg  $\text{InCl}_3$ , and 300 mg TAA were added after stirring and stirred for another 15 min. After that, it was transferred to an oil bath and stirred at 80 °C for 4 h. The yellow precipitate obtained was washed with ethanol and dried at 50 °C for 12 h. The yellow precipitate obtained was washed with ethanol and dried under vacuum at 50 °C for 12 h. The successful ZnS/ZIS prepared in different ratios are referred to as 100-ZnS/ZIS, 75-ZnS/ZIS, 50-ZnS/ZIS and 25-ZnS/ZIS, respectively. The process is diagrammed in Fig. 1.

### 2.3. Characterization

Scanning Electron Microscope (SEM, Hitachi-Hitachi SU 8020, Japan; Energy Spectroscopy, HORIBA EX250-Horiba, Japan) and Transmission Electron Microscope (TEM, FEI Tal os F200X) were utilized for the material micro-morphology testing.

X-ray diffraction (XRD, Bruker D8 ADVANCE, Germany, Cu and Co target wavelengths are 1.5406 Å and 1.79026 Å) and X-ray photoelectron spectroscopy (XPS, Thermo scalable 250XI, USA) were tested for the crystalline structure of the material, proving the successful preparation of the material.

For testing the photocatalytic properties of the materials, UV diffuse reflectance, physical adsorption test, photoluminescence spectroscopy, and electrochemical workstation were conducted. Physical adsorption tests were performed using the Mac ASAP 2460 test. Photoluminescence (PL) spectroscopy was analyzed using the Edinburgh FLS1000/FS5 with an excitation wavelength of 330 nm. The excitation wavelength was the same as that of the FLS1000/FS5, and temporally resolved transient concentrator decay curves were measured at approximately 450 nm. All electrochemical experiments were performed on an electrochemical workstation (CHI-660E). EPR tests were performed using a JES-FA200 (JEOL) ESR spectrometer at X-band frequency at room temperature. UV X-ray photoelectron spectroscopy tests were performed on a Thermo scalable 250XI instrument at monochromatic Al K $\alpha$  ( $h\nu = 1486.6$  eV).

### 2.4. Photocatalytic activity tests

Assessment of the photocatalytic activity of the samples was carried out under the irradiation of a xenon lamp and a UV-cut filter. Typically, 10 mL of HMF (2 mM) aqueous solution and 20 mg of catalyst were incorporated into a 50 mL quartz photoreactor.

Thereafter, the reactor was swirled vigorously (600 rpm) for 30 min in all darkness to ensure the possibility of adsorption or reaction. Connect a water condenser and make sure that the reaction system is kept at 20 °C. The reaction was continued under light and stirring. The process was run under light and constant stirring for 6 h. The samples were collected at 30 min and 6 h, respectively, and placed in liquid-phase sealed vials for analysis.



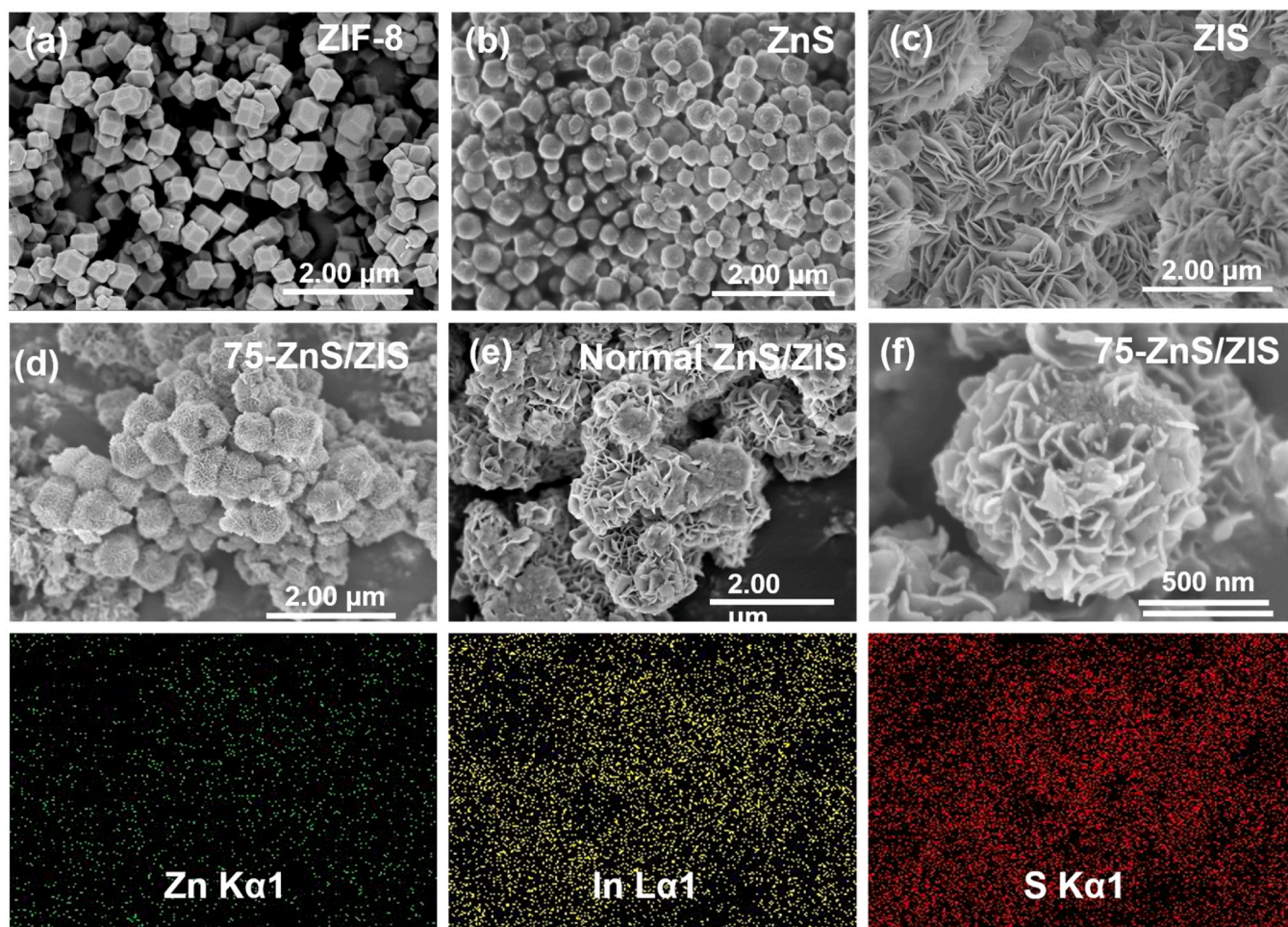


**Fig. 2.** Scanning electron microscope images of ZIF-8 (a), ZnS (b), ZIS (c), 75-ZnS/ZIS (d), Normal ZnS/ZIS (e) and EDS elemental maps of zinc, indium and sulfur for 75-ZnS/ZIS (f).

Sample concentration was quantified by peak intensity in a high performance liquid chromatography (HPLC) system equipped with an RID detector using an organic acid column (Aminex HPX-87H) with 4 mM sulfuric acid as the mobile phase at a flowing speed of 0.6 mL/min.

$$Conv_{HMF} = \frac{C_{HMF,0} - C_{HMF}}{C_{HMF,0}} \times 100\%$$

$$Yield_{DFF} = \frac{C_{DFF}}{C_{DFF,1}} \times 100\%$$

$$Select_{DFF} = \frac{Yield_{DFF}}{Conv_{HMF}} \times 100\%$$

Where,  $C_{HMF,0}$  is the initial concentration of HMF;  $C_{HMF}$  and  $C_{DFF}$  are the concentrations of HMF and DFF, respectively, after the reaction;  $C_{DFF,1}$  is the theoretical concentration of DFF after the completion of HMF conversion.

The detection of  $H_2O_2$  was measured by the  $[TiO(H_2O_2)]^{2+}$  chromogenic agent-spectrophotometer method, and the yield of  $H_2O_2$  could be calculated using the standard curve prepared in advance as the base point.

### 3. Results and discussion

#### 3.1. Morphology, structure, and optical property

Morphologies and structures of the fabricated photocatalysts can be attained by SEM and TEM. The precursor ZIF-8 was synthesized by a modified precipitation method and exhibits an ortho-dodecahedral geometry (Fig. 2a). The hollow ZnS structure was then prepared by sulfur etching it. In the vulcanization process, sulfide ions released by TAA were driven by high temperature and high pressure to react with Zn ions in ZIF-8 to generate ZnS in the outer layer, and then slowly erode to the inner layer to finally generate ZnS hollow structure[20]. Fig. 2b verifies the hollow structure of ZnS, which is found to inherit the ortho-decahedral morphology of ZIF-8. The morphology of pure ZIS nanosheets is shown in Fig. 2c. In the loaded ZIS process, the cations were first adsorbed on the surface of ZnS by the Coulomb force and then reacted with the sulfide ions released from TAA to grow ZIS particles on the surface of ZnS, which tightly encapsulated ZnS. Fig. 2d displays the ZnS/ZIS composites formed after applying a further coating of ZIS nanosheets. The hollow properties can also be directly observed in the partial fragmentation of the samples in Fig. 2b and d. Normal particles of ZnS and ZIS are unevenly combined to form a non-hollow composite structure (Fig. 2e). Further scaling up of the hollow ZnS/ZIS nanoreactor observed that a large number of flakes with a thickness of a few nanometers were loaded on the surface of the shell, like flourishing dandelions. To study the elemental components and distribution of ZnS/ZIS, the associated elemental maps were tested with different colors to



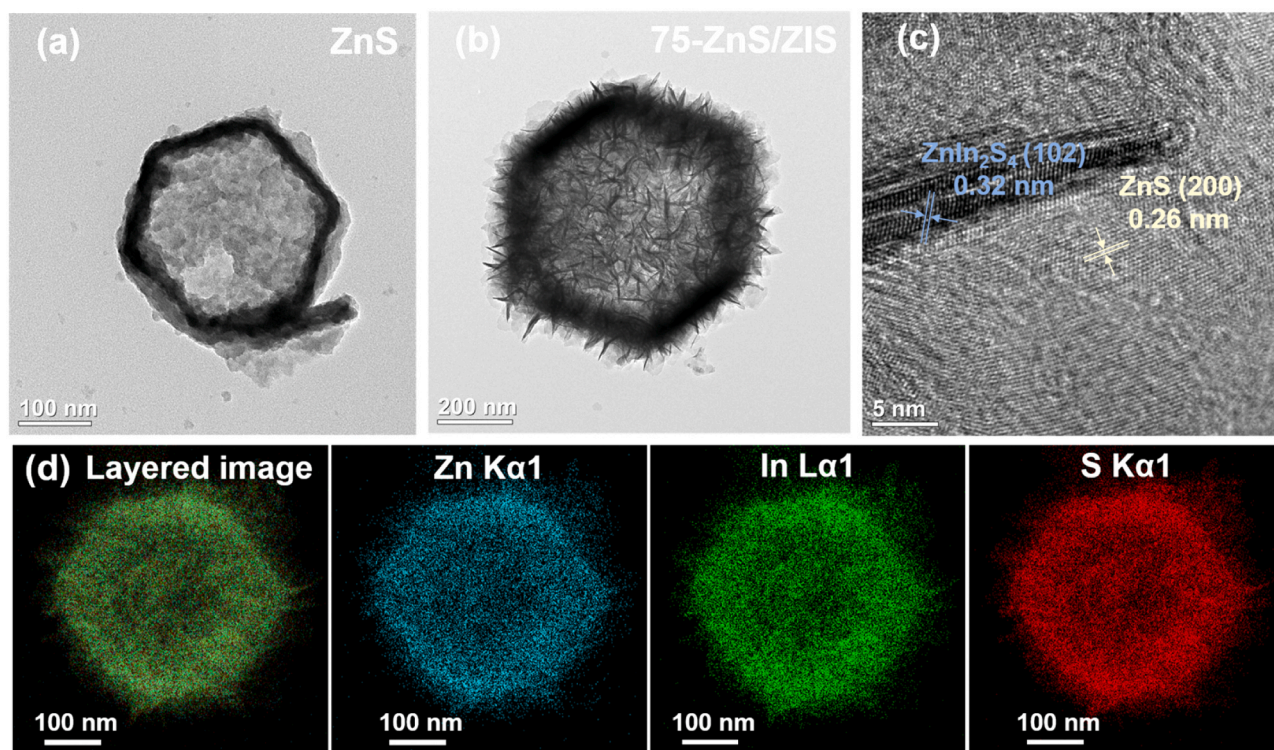


Fig. 3. TEM image of ZnS (a), 75-ZnS/ZIS (b), HRTEM image of 75-ZnS/ZIS (c), and the EDS elemental mappings of Zinc, Indium, and Sulfur of 75-ZnS/ZIS (d).

indicate the existence of Zn, In and S elements. The SEM image contours confirming the homogeneous dispersion of all elements are shown in Fig. 2f. The electron spectra of SEM elements are illustrated in Fig. S1, and the atomic percentages of Zn K, In L, and S K are 19.47 %, 26.05 %, and 54.48 %, correspondingly. SEM-EDX elemental analysis demonstrated that ZnS and ZIS were successfully co-loaded to form ZnS/ZIS.

Moreover, the comparison of ZnS/ZIS morphology with different doping amounts was observed with TEM. The hollow structures in Fig. 3a demonstrate the success of ZnS dodecahedral hollow shell etching. As shown in Fig. S2, ZIS presented a lamellar structure with ultrathin properties, and ZIS grew staggered on ZnS to form composite nanomaterials. This structure tends to increase the specific surface area of the catalyst and forms a heterogeneous configuration. However, when the ZnS doping is large (100 mg, Fig. S2 a), the composites are prone to non-uniform ZIS loading and ZIS may easily agglomerate on its own

without compositing with ZnS, while low doping (25–50 mg, Fig. S2 c-d) will trigger a significant amount of ZIS to cover the hollow shell thus reducing the chance of exposure of the overall active sites of the catalyst. Proper doping increases the probability of contact between the material and the reactants and boosts the catalytic activity. Fig. 3c shows a high-resolution TEM (HRTEM) image of 75-ZnS/ZIS, indicating that the synthesized photocatalysts are polycrystalline in structure, and (102) planes (with a lattice spacing of 0.32 nm) corresponding to ZIS [21] and (200) lattice planes (0.26 nm) corresponding to ZnS [22] were observed, suggesting that the two materials were in close contact and successfully generated heterostructures. The three elements, Zn, In, and S, were equally distributed under the HAADF-STEM elemental mapping (Fig. 3d), which further demonstrated the successful synthesis of the ZnS/ZIS heterostructure. The above test outcomes show a homogeneous and intimate coupling between ZnS and ZIS at the microscopic level,

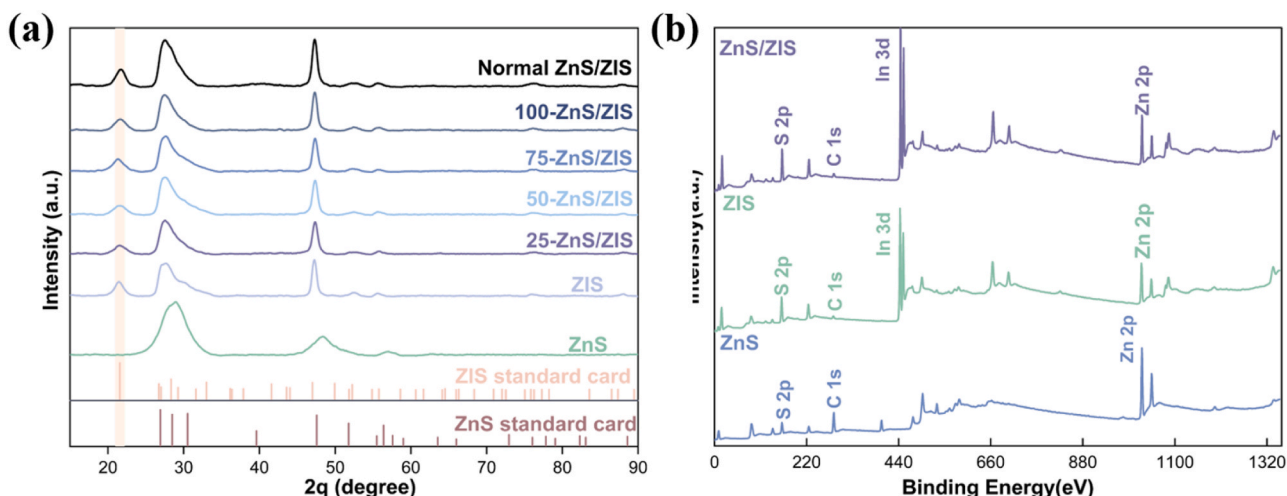


Fig. 4. X-ray diffraction (XRD) of different catalysts (a), X-ray photoelectron spectroscopy (XPS) of ZnS/ZIS, ZnS, and ZIS (b).



which means that a nanoscale ZnS/ZIS heterostructure has been successfully formed. The hollow structure inherently has a high specific surface area, and the composite remedies the defect of the small contact area of ZIS, providing a higher reactive site for the reaction.

The crystal structures of synthesized ZnS, ZIS, and ZIS with ZnS doping ratios ranging from 100 to 25, as well as non-hollow ZnS/ZIS, were tested by X-ray diffraction (XRD) analysis and the results are given in Fig. 4a. Generalized diffraction peaks of ZnS and ZIS were noted in the heterogeneous structure and standard cards of both were used as a comparison. The diffraction peaks of ZIS are located at 21.5°, 28.8°, 47.3°, 52.2°, and 56.4°, and the six peaks correspond to the crystallographic planes (006), (103), (110), (1012), and (203) of a typical cubic ZIS (JCPDS NO. 72–0773)[21,23], which proves the elemental presence states. For ZnS nanosheets, the diffraction peaks at 28.0°, 48.8°, and 56.8° closely match the (111), (220), and (311) crystal planes of typical cubic ZnS (JCPDS NO. 80–0007)[23].

The elemental composition of the base materials ZnS and ZIS and the composite ZnS/ZIS as well as the surface elemental states were characterized by X-ray photoelectron spectroscopy (XPS) analysis (Fig. 4b). The total XPS scanning spectra showed peaks attributable to the elements Zn, In, and S, proving that the composite comprised the elements Zn, In, and S. In Fig. S3, the Zn 2p peaks in the three species are at positions around 1021 eV and 1044 eV attributed to Zn 2p<sub>1/2</sub>, Zn 2p<sub>3/2</sub>, the S 2p orbital peaks are at positions 161 eV and 162 eV attributed to S 2p<sub>1/2</sub> and S 2p<sub>3/2</sub>, and the spectral peaks of In 3d are at positions 444 eV and 452 eV attributed to In 2p<sub>3/2</sub> and In 2p<sub>5/2</sub>. The peak positions are in agreement with other literature results[22,23]. The absence of diffraction peaks corresponding to impurities further confirmed the phase purity of the prepared photocatalysts, and the ZnS/ZIS heterostructures exhibited a highly crystalline state by XRD. By comparison, it is found that the binding energy of the elements changes after the construction of the heterojunction, which is due to the strong interaction between ZIS and ZnS. The in situ XPS results for the element In show a shift of electrons in the direction of ZIS in visible light (Fig.S4), which is consistent with the above inferences. The characterized structure can be a theoretical basis for the successful construction of the heterostructure.

To fully endorse the XPS and XRD results, we investigated the actual content of elements in 75-ZnS/ZIS based on TEM Energy Dispersive X-Ray Spectroscopy (TEM-EDX) spectroscopy (Fig. S5). The results showed that the contents of Zn, In and S were 27.3 %, 27.0 % and 45.7 %, respectively, which indicated that ZnS and ZIS had been successfully integrated. This is slightly different from the SEM energy-sweep results (19.47, 26.05 and 54.48 % for Zn, In and S, in SEM-EDX results), however in agreement with theory and speculation. SEM performed elemental scanning of the material surface and TEM obtained the elemental distribution throughout the material by penetration. The percentage of Zn and S elements in the TEM increases and decreases, and there is a slight increase in In elements, respectively. Because the ZnS shells covered by the ZIS on the surface are observed in the transmission view, each ZIS nanosheet stacked together can be scanned, so the Zn and In elements are more from the results, and the S element decreases relatively. Based on the above experimental results, it is proved that a hollow ZIS/ZS heterojunction structure has been successfully prepared.

### 3.2. Performance analysis of photocatalytic selective oxidation of biomass

To validate the enhancement of photocatalytic performance by ZnS/ZIS heterostructures and the hidden potential application of heterostructures based on ZnS-based hollow nanoreactors in biomass valorization, a visual light-driven catalytic transformation of HMF was carried out at room temperature and under mild conditions without any other additives using atmospheric oxygen as an oxidant. After 6 h of reaction, the pure ZnS samples (plain particles and hollow material) did not demonstrate catalytic activity. The HMF conversion of the primitive ZIS material under visible light irradiation was 41.51 %, with a selectivity of 67.64 % and a yield of 28.08 % for DFF. The cause of the low

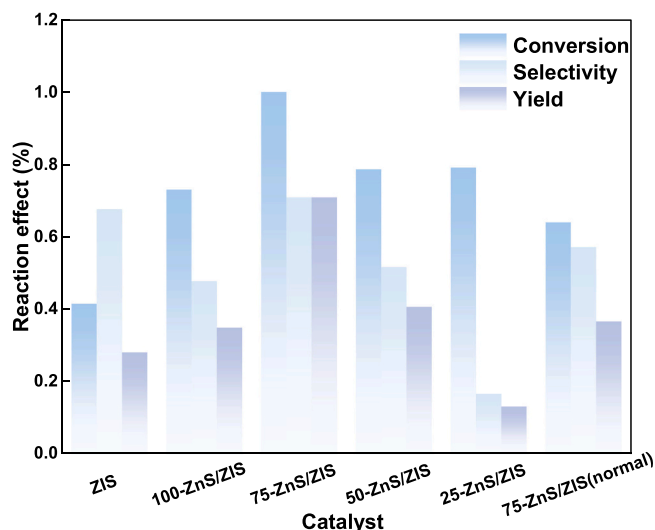


Fig. 5. Photocatalytic HMF to DFF with different catalysts.

Table 1

Comparative results with other studies.

| Catalyst              | Solvent | Reaction Conditions   | Conv. (%) | Select. (%) | Yield (%) |
|-----------------------|---------|---|-----------|-------------|-----------|
| ZnS/ZIS               | Water   | 500 W Xe lamp ( $\lambda > 420$ nm), 20 °C, under air, 6 h  | 100       | 70.9        | 70.9      |
| MNs/CIS [25]          | Water   | 500 W Xe lamp ( $\lambda > 420$ nm), 20 °C, under air, 12 h | 78.5      | 76.8        | 60.3      |
| Cd1.5In2S4.5 [26]     | Water   | 500 W Xe lamp ( $\lambda > 420$ nm), 20 °C, under air, 6 h  | 68.8      | 62.7        | 43.2      |
| V2O5-nH2O/g-C3N4 [27] | Water   | Visible light, 4 h  | 42.5      | 84          | 35.7      |
| Fe(III)/Bi2MoO6 [28]  | Water   | 500 W Xe lamp ( $\lambda > 400$ nm)                         | 32.6      | 95.3        | 31.1      |
| CTF-Th@SBA-15 [29]    | Water   | Blue LED ( $\lambda = 460$ nm)                              | 57.0      | 99.0        | 56.4      |
| TE-520-P25 [30]       | Water   | Fluorescent lamp ( $\lambda = 340-420$ nm)                  | 50        | 35          | 17.5      |

photocatalytic activity is that the photogenerated  $e^-h^+$  pairs undergo drastic recombination, and both diffusion and recombination are made facile by the short-range electron and hole transport paths that result from the nanosheet's ultrathin structure.

The photocatalytic activity of the heterogeneous structure was successfully promoted after the composite of hollow structures. The photocatalytic oxidation of HMF by 100-ZnS/ZIS, 75-ZnS/ZIS, 50-ZnS/ZIS, 25-ZnS/ZIS and non-hollow ZnS/ZIS resulted in the conversion of HMF of 73.1 %, 100 %, 78.6 %, 79.1 % and 64 %, and the yield of DFF of 47.7 %, 70.9 %, 51.7 %, 16.6 % and 57.2 %, respectively (Fig. 5). The best properties of the hollow 75-ZnS/ZIS heterostructure were attributed to the advantageous establishment of the ZnS hollow structure and the optimal ratio of the two materials, the interfacial effect of the 75-ZnS/ZIS heterostructure, and the efficient charge transfer. The reaction efficiency of the non-hollow composites (conversion 64.01 %, selectivity 57.20 %, yield 36.62 %) is much worse than that of the hollow (with the same material doping ratio), which indicates that the purely heterogeneous structure building does not accomplish the optimization of the reaction effect, and directly illustrates the predominance of the hollow nanoreactor. It was also found that the photocatalytic activity was inferior when the ZnS level was too low. The suppressed effect of the composites, in this case, could be attributed to the fact that a significant

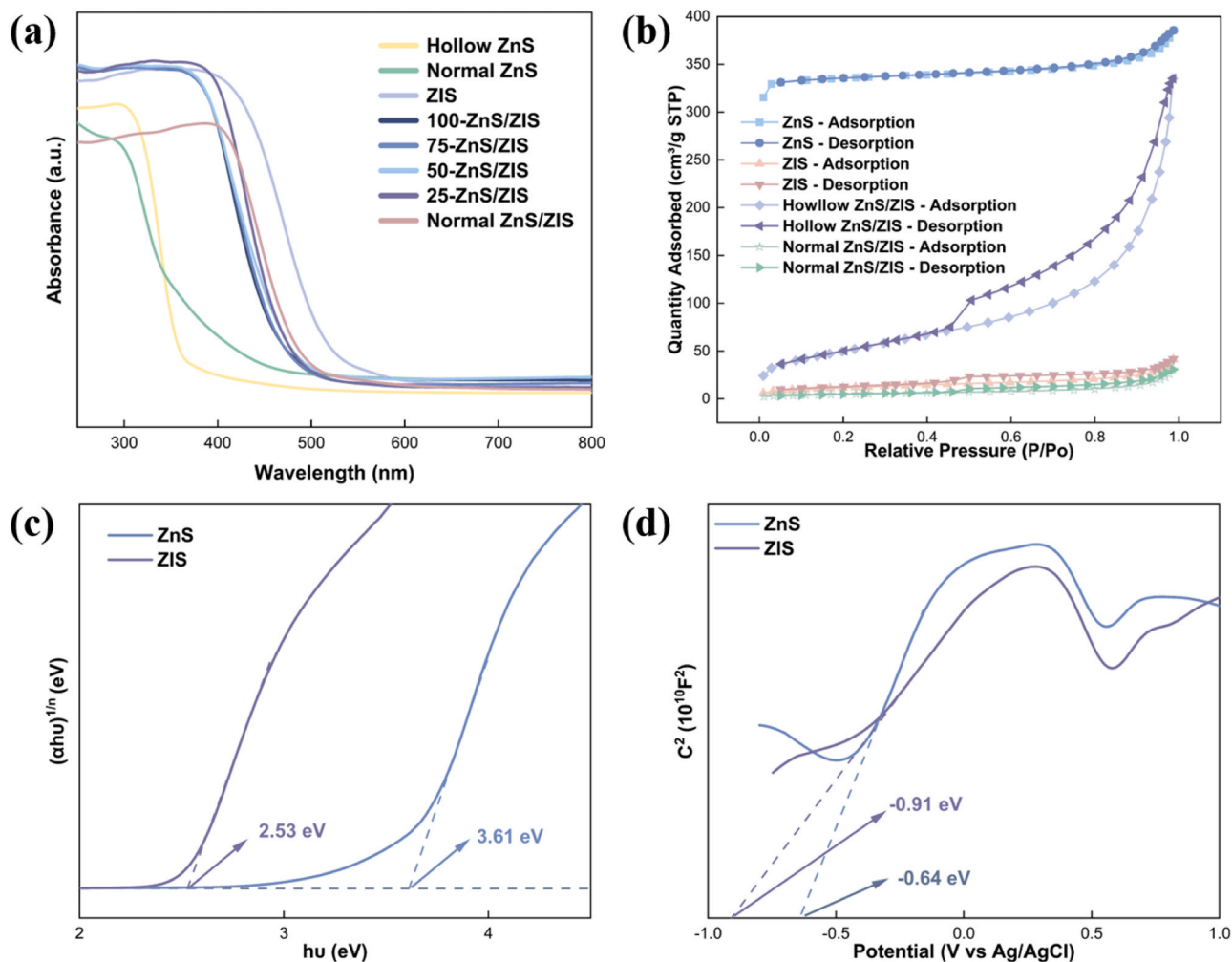


Fig. 6. UV-vis-NIR DRS spectra (a), Isothermal adsorption test (b), Photon energy of ZnS and ZIS (c), the Mott-Schottky measurement of ZnS and ZIS (d).

number of ZIS were stacked on the same dodecahedral hollow ZnS. The coverage between ZIS and ZnS led to the light shielding effect. The overall light utilization efficiency of the catalyst was diminished, leading to a decrease in photoactivity, which is also verified in the TEM characterization results (Fig. S2). The appropriate material occupancy ratio brings about a well-distributed heterogeneous structure.

Table 1 shows that the catalytic transformation efficiency of the 75-ZnS/ZIS heterostructure for HMF is much better than that of other photocatalytic systems, when the experiments were also conducted under atmospheric conditions, especially in terms of yield, which is significantly different from the results of other studies. Accurate assessment of the catalyst's stability is crucial for its development in photocatalysis, so the best material, 75-ZnS/ZIS, was investigated by repeated use of five consecutive experiments (Fig. S6). The results showed that the catalytic effect of HMF on 75-ZnS/ZIS remained almost invariable, suggesting that the constructed heterogeneous structure has better stability and repeated usability. The aforementioned characterization SEM, XPS, XRD and catalysis experiments verified the micro-morphology and stability of the crystal structure of 75-ZnS/ZIS. The photogenerated electron-hole transfer along the heterostructure interface under the excitation of visible light irradiation and the efficient channeling allows for a rapid carrier depletion reducing the photocorrosion of the metal sulfide, which results in an outstanding robustness of the 75-ZnS/ZIS heterostructure [24]. Meanwhile, ZnS/ZIS has good generalisability to biomass, including glucose, benzyl alcohol, and furfuryl alcohol (Table S1).

### 3.3. Photogenerated carrier transport performance measurement

The absorption efficiency of the synthesized catalysts for different wavelengths of light was reflected by ultraviolet visible diffuse reflectance (DRS) (Fig. 6a). The property that ZnS can only absorb high-energy photons may be the reason for its inability to convert HMF in visible light. However, compared with granular ZnS, hollow ZnS has a stronger light absorption capacity due to internal refraction. This is reflected in the UV-DRS spectra (Fig. 6a), where long straight lines with greater slopes in the vertical direction represent stronger light absorption in this band. Both granular ZnS and normal ZnS/ZIS have weaker light absorption in different bands than the hollow type of materials. The higher the percentage of ZIS in different ratios of ZnS/ZIS composites, the more pronounced the trend of red-shifting of the catalyst absorption edge. Thus the Burstein-Moss effect occurred giving the substance a doping effect in the hybridization process [31]. The absorption position of the 75-ZnS/ZIS sample is around 470 nm (Fig. S7), which is ascribed to the strong light-absorbing nature of hollow ZnS and the efficient utilization of sunlight by ZIS. This finding suggests that the hollow heterostructure ZnS/ZIS is able to collect more solar spectrum in range and more light energy of the same wavelength band in intensity, and its excellent visible light absorptivity will provide a solid guarantee to promote its photocatalytic activity.

The isothermal adsorption and desorption tests were also carried out for ZnS, ZIS and hollow and non-hollow ZnS/ZIS, and their BET-specific surface areas were 1006.31 m<sup>2</sup>/g, 41.10 m<sup>2</sup>/g, 184.47 m<sup>2</sup>/g and 18.18 m<sup>2</sup>/g, respectively. The great improvement in material area



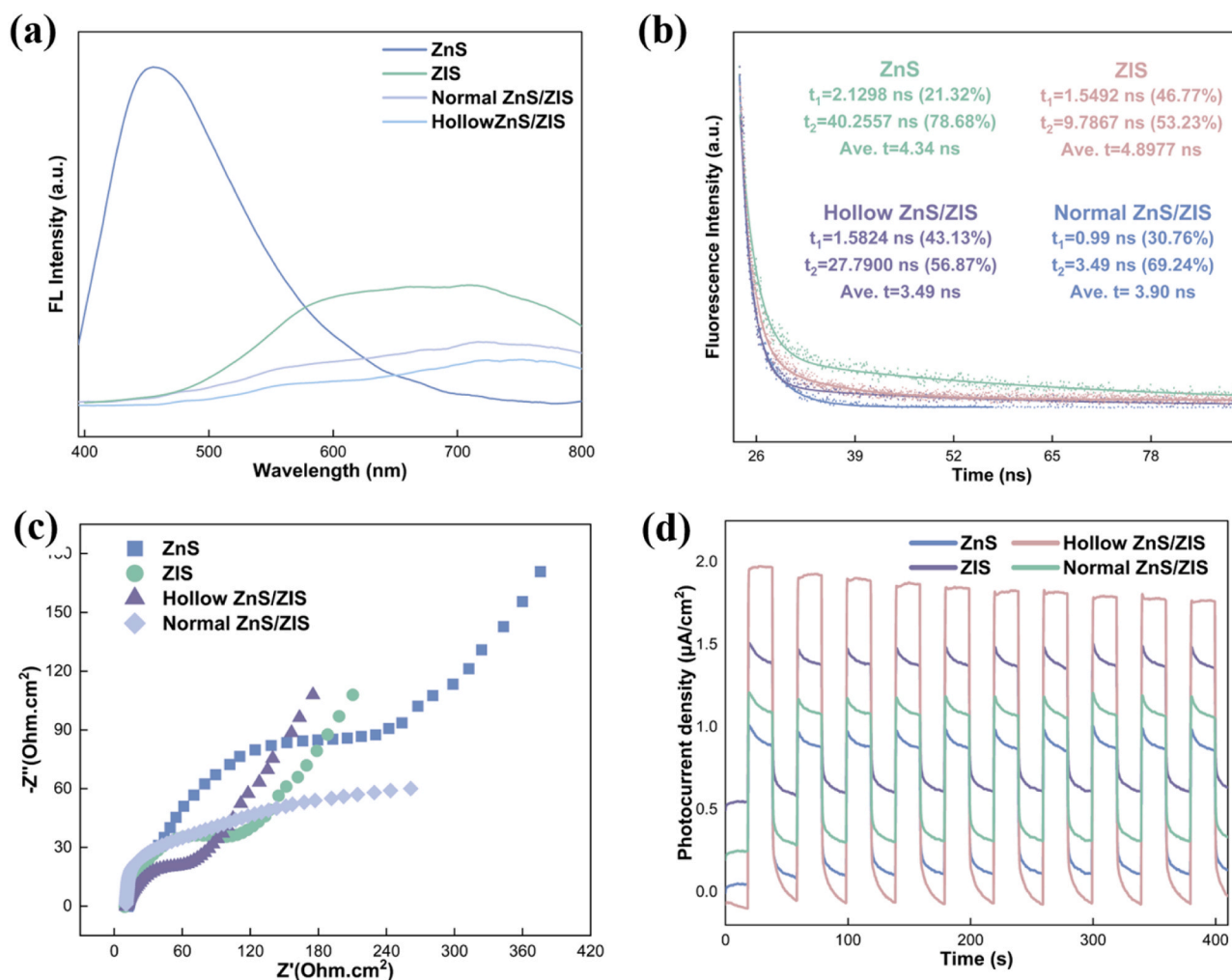


**Fig. 7.** Photoluminescence spectroscopy (PL) (a), Fluorescence life (b), Photoelectrochemical impedance diagram (c) and photocurrent response of the photocatalyst (d).

brought about by the dodecahedral hollow structure of ZnS can be visualized in Fig. 6b. Despite constituting a heterogeneous structure, the extremely low surface area of ordinary ZnS does not favour its reaction. An increase in the specific surface area of ZnS/ZIS by a factor of 4.5 was observed in comparison with ZIS. Combined with the performance of the materials in the light-free dark reaction, the materials (ZnS, ZIS, and hollow ZnS/ZIS) adsorbed 4.10, 1.21, and 2.36 %, respectively, exhibiting adsorption properties consistent with the results of the isothermal adsorption test. This indicated that a higher surface area not only helps the catalyst material to provide more attachment opportunities for the reaction substrate during the catalytic process but also exposes the active site for further contact.

The energy band structure matching with the reaction is a key factor in ensuring a fluent photocatalytic reaction. As depicted in the plot of  $(\alpha h\nu)^{1/2}$  versus photon energy for ZnS and ZIS in Fig. 6c, the band gaps of ZnS and ZIS were analyzed and processed to be 3.61 eV and 2.53 eV, respectively. The work functions of ZnS and ZIS were further determined by Mott-Schottky curves (M-S curves) and ultraviolet photoelectron spectrum (UPS). As shown in Fig. 6d, the M-S curves of the two materials have positive slopes, thus proving that ZnS and ZIS are n-type semiconductors [32]. Taking the longest straight line that can be found on the M-S line as a tangent to the x-axis, one can derive flat band potentials are about  $-0.64$  eV and  $-0.91$  eV (to Ag/AgCl). The conduction band (CB) edges of n-type semiconductors are considered to be close to their flat-band potentials [33], so the conduction band are estimated to be

$-0.44$  and  $-0.71$  eV (to NHE), and the valence band (VB) potentials are calculated according to the following equations:

$$E_{VB} = E_g - E_{CB}$$

Valence band calculations resulted in 3.17 and 1.82 eV (relative to NHE). After extrapolating the UPS results to obtain (Text S1), the ZnS and ZIS work functions ( $\Phi$ ) are 4.62 and 3.63 eV (relative to the absolute vacuum scale). The work function is numerically equal to the difference between the vacuum level ( $E_{vac}$ ) and the Fermi level ( $E_F$ ):

$$\phi = E_{vac} - E_F$$

A higher work function corresponds to a lower Fermi energy level, so ZnS with low Fermi energy levels implies a greater ability to bind electrons. When the interfaces of the two are in close contact, the electrons on ZIS should be spontaneously transferred to ZnS at the heterojunction interface until the  $E_F$  of ZnS rises to the same level as that of ZIS. The binding energies of the Zn 2p, In 3d, and S 2p orbitals of ZnS/ZIS are negatively shifted compared to ZIS and positively shifted compared to ZnS in high-resolution XPS spectroscopy (Fig. S3 and Fig. S4), suggesting that the electrons are transferred from ZIS to ZnS under the action of the heterojunction, which agrees with the above inference. During the electron transfer process, the Fermi energy levels gradually reached equilibrium and the region near the ZnS/ZIS interface was charged. As electrons were lost from ZIS and gained by ZnS, an internal electric field from ZIS to ZnS was established, which could dramatically speed up the

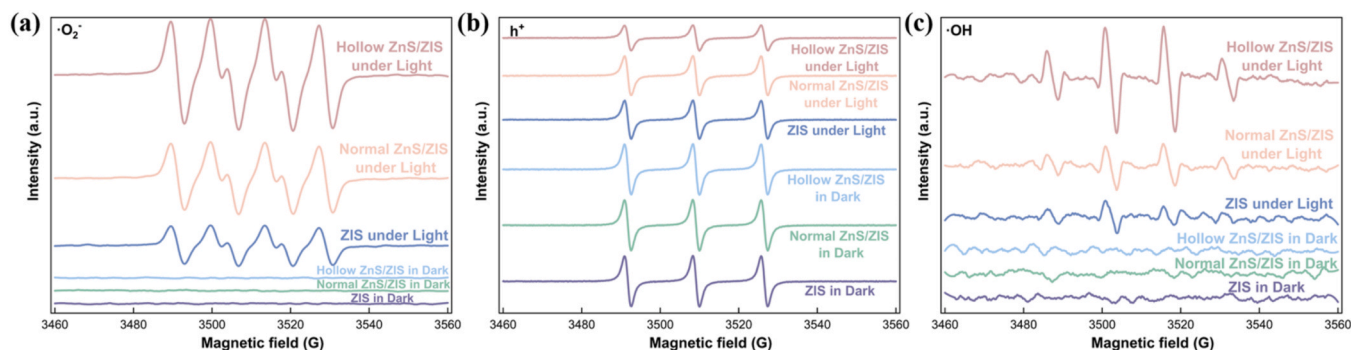


Fig. 8. Electron Paramagnetic Resonance (EPR) of  $\cdot\text{O}_2^-$  (a),  $h^+$  (b) and  $\cdot\text{OH}$  (c).

electron jump from the conduction band of ZnS to the valence band of ZIS under photoexcitation [34,35]. During this process, the energy bands of ZnS are bent downward owing to electron accumulation, while ZIS is bent upward owing to the loss of electrons [36]. An S-scheme photogenerated carrier migration mechanism was successfully proposed. When the sample is excited by visible light, affected by the internal electric field and the energy band bending effect, the hoarded electrons on the ZnS conduction band migrate to the ZIS valence band, the electrons on the ZIS conduction band and the holes on the ZnS valence band get enriched, and S-scheme heterojunction formed effectively separates the photogenerated carriers and inhibits the recombination of photogenerated electron-hole pairs, thus promoting the photocatalytic activity of the composites.

To further verify the enhancement of the photoelectric properties of the composites by constructing the heterojunction structure, the photoelectrochemical properties were tested. Photoluminescence spectroscopy (PL) was employed to analyze the photogenerated carrier separation and migration efficiencies as well as the recombination rates of electron-hole pairs of the prepared catalysts (Fig. 7a) to investigate the effect of doping of the two materials. Theoretically, hole and electron recombination transients on photocatalyst samples lead to greater PL peak intensities [37]. In several test results, significant peak intensities were detected in the PL spectra of ZnS and ZIS, whereas the peak intensities of the composite ZnS/ZIS materials (hollow and non-hollow) were smaller, suggesting that the composites can rapidly transfer excited state electrons under the dominance of the heterojunction, a trend reinforced by the hollow structure. This results in a rapid separation of light-induced electron-hole pairs, which reduces the recombination probability and thus the hardening strength of the PL spectra. The average concentrator decay time ( $\tau_{\text{average}}$ ) of hollow ZnS/ZIS nanoreactors was 3.49 ns, and 3.90 ns for the normal ZnS/ZIS, which were both lower than that of the base ZnS material (4.34 ns) and the ZIS material (4.90 ns) (Fig. 7b). In contrast, the decay rate of normal ZnS/ZIS is significantly faster than that of ZnS and ZIS, and the fluorescence lifetime of the hollow material is even shorter, which reveals that the composites have adopted an unusual attenuation method in addition to the conventional attenuation, i.e., the carrier recombination process is effectively suppressed by transferring to the acceptor material and thus separating the carriers successfully, which is facilitated by structural advantages of the hollow material. In accordance with the EIS test, the charge transfer capacity of solid interfaces has also been examined, which is an important tool for studying the kinetics of catalytic processes and surface phenomena [36]. The comparative results of the arc radii in Fig. 7c show that the hollow ZnS/ZIS radius is the smallest, indicating that the material has the best  $e^-h^+$  pair separation and presents the lowest photoelectric impedance, which suggests that the heterogeneous structure gives the material excellent electrical conductivity and carrier mobility. The transient photocurrent spectroscopy results further support these conclusions. The higher photocurrent density of hollow ZnS/ZIS compared to ZnS, ZIS and non-hollow

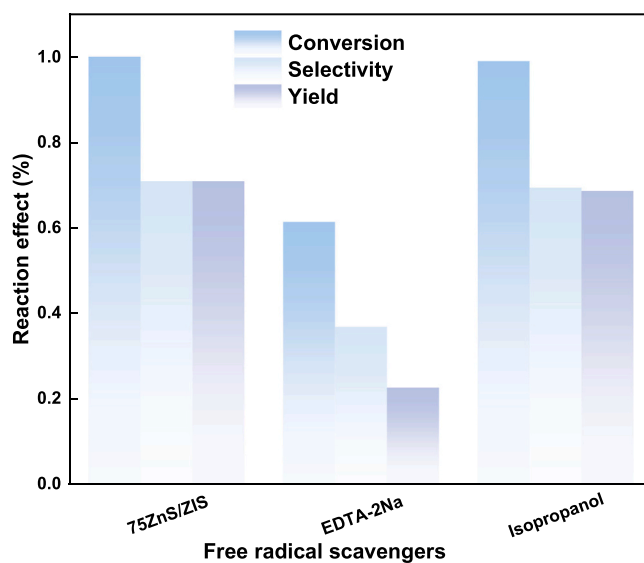


Fig. 9. Reactive Free Radical Capture Experiment of 75-ZnS/ZIS.

materials demonstrates that its hollow heterostructure improves the visible light responsiveness and speed of the material and provides a convenient delivery channel for photogenerated carriers (Fig. 7d).

### 3.4. Reaction mechanism inference

In general, the active radicals in the photocatalytic aqueous-phase system are primarily superoxide free radicals ( $\cdot\text{O}_2^-$ ), holes and hydroxyl free radicals ( $\cdot\text{OH}$ ). To confirm the type and amount of reactive radicals in it, the active species were examined.

Electron paramagnetic resonance (EPR) tests were done for the possible presence of reactive radicals in the reaction system. Superoxide radicals and hydroxyl radicals were used 5,5-dimethyl-1-pyrroline-N-oxide (DMPO) as a trapping agent and 2,2,6,6-tetramethylpiperidinyloxy (TEMPO) as a hole trapping agent. It is important to note that TEMPO is a paramagnetic, persistent radical that has an EPR signal of its own, and the hole on the catalyst surface combines with its surface single electron to reduce the signal as evidence of hole generation. As illustrated in Fig. 8, since there is a positive relationship between the number of free radicals and the squares of the  $\cdot\text{O}_2^-$  and  $\cdot\text{OH}$  signal intensities [38], the absence of signals under dark conditions indicates that the reaction did not take place in the absence of light conditions. The  $h^+$  characteristic peak is obvious under darkness, which follows the theory. Under simulated daylight conditions, the ordering of all three active radical concentrations of the photocatalysts was Hollow ZnS/ZIS > Normal ZnS/ZIS > ZIS, and the comparison of the  $h^+$  and  $\cdot\text{OH}$  of Normal ZnS/ZIS and ZIS is further labeled in Fig. S8. The experimental



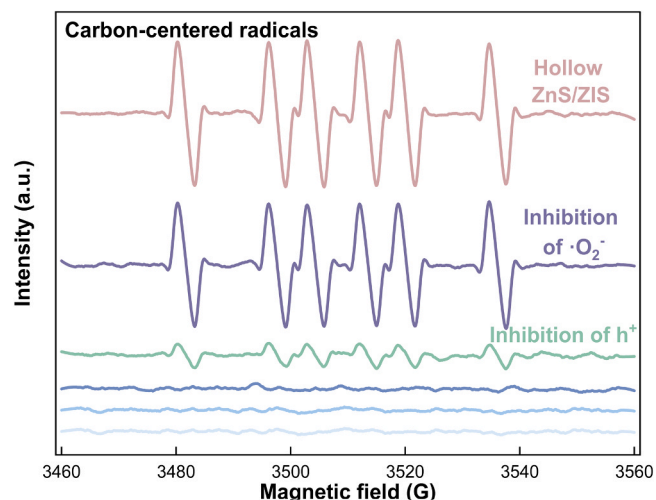


Fig. 10. Carbon-centred radical generation under different conditions.

results support the conclusion that the heterogeneous structure of ZnS/ZIS significantly increases the formation efficiency of photo-generated carriers, and the hollow structure further strengthens the light-absorption efficiency, which leads to a gradual increase in the concentration of reactive radicals.

Trap agent experiments assist in identifying the main reactive radicals that function in the catalysis of HMF (Fig. 9). P-benzoquinone (PBQ), ethylenediamine tetraacetic acid disodium salt (EDTA-2Na), and isopropanol (IPA) were chosen as removers of  $\cdot\text{O}_2^-$ ,  $\text{h}^+$ , and  $\cdot\text{OH}$ , separately, and the concentration of each trapping agent was  $10^{-3}$  mol/L in the reaction system. After adding PBQ, the reaction almost completely stopped, indicating that  $\cdot\text{O}_2^-$  is the dominant reactive radical for the organization of HMF oxidation to DFF in the aqueous system.  $\cdot\text{OH}$  did not have an impact on the reaction, which is consistent with the findings of others that despite  $\cdot\text{OH}$  having the strongest oxidising capacity of the three radicals, its incompatibility with the HMF oxidation reaction leads to redundancy. The incorporation of  $\text{h}^+$  traps has been reported to

enhance photocatalytic efficiency by preventing photogenerated  $\text{e}^-$ - $\text{h}^+$  pairs from recombining under general conditions [20]. However, this trend was not exhibited in the hollow ZnS/ZIS nanoreactor, which not only indicated that the S-scheme heterojunction achieved efficient separation of photogenerated electron-hole pairs, but also suggested that  $\text{h}^+$  might play an essential role in the reaction. Furthermore, the reaction did not proceed under argon atmosphere, indicating that atmospheric  $\text{O}_2$  is the oxidising agent for the reaction.

The oxidation of HMF to DFF begins with the hydroxyl group shedding a hydrogen atom, during which there is a high probability that alcoholate anion intermediates will be generated, as evidenced by the results of the EPR (Fig. 10). The intermediate signal peaks were found to be sharply weakened by the addition of the  $\text{h}^+$  trapping agent to the reaction system, unlike the addition of the  $\cdot\text{O}_2^-$  trapping agent where the intensity of the signal peaks was close to that without any addition of the trapping agent. This illustrates that the oxidation pathway of HMF is captured by  $\text{h}^+$  to first generate alcoholate anion radicals, and the superoxide radicals react with the  $\text{H}^+$  removed by HMF to generate  $\cdot\text{OOH}$  radicals, which are further oxidised to DFF as well as the by-products  $\text{H}_2\text{O}_2$ , and the results of the tests of  $\cdot\text{OOH}$  and  $\text{H}_2\text{O}_2$  are supported by Fig. S9 as well as by the chromogenic reaction of the colour developing agent,  $[\text{TiO}(\text{H}_2\text{O}_2)]^{2+}$  (Table S2). After the capture of  $\text{h}^+$ , the HMF is directly exposed to the strongly oxidising  $\cdot\text{O}_2^-$ , which is partially mineralised directly to  $\text{CO}_2$ , leading to a decrease of selectivity, which is supported by the decrease of elemental C in the TOC results (Table S3), suggesting that synergistic action of the two reactive radicals is more favourable for the reaction.

In light of the adequate characterisation tests described above and supported by results from other literature [36,39], it is possible to deduce a mechanism for the oxidation of HMF to DFF using atmospheric oxygen in the hollow ZnS/ZIS heterostructure-water-phase system. In the non-reactive state, electrons in the heterostructure tend to transfer from ZIS to ZnS, where they are more tightly bound. Under visible light irradiation, ZnS and ZIS generate photo-generated  $\text{h}^+$  and  $\text{e}^-$ . Due to the higher work function of ZnS, the energy band of ZnS bends downward while that of ZIS bends upward, forming a classical S-scheme heterostructure. The electrons on ZnS conduction band are transferred to holes on ZIS valence band, and the electrons on ZIS combine with oxygen in

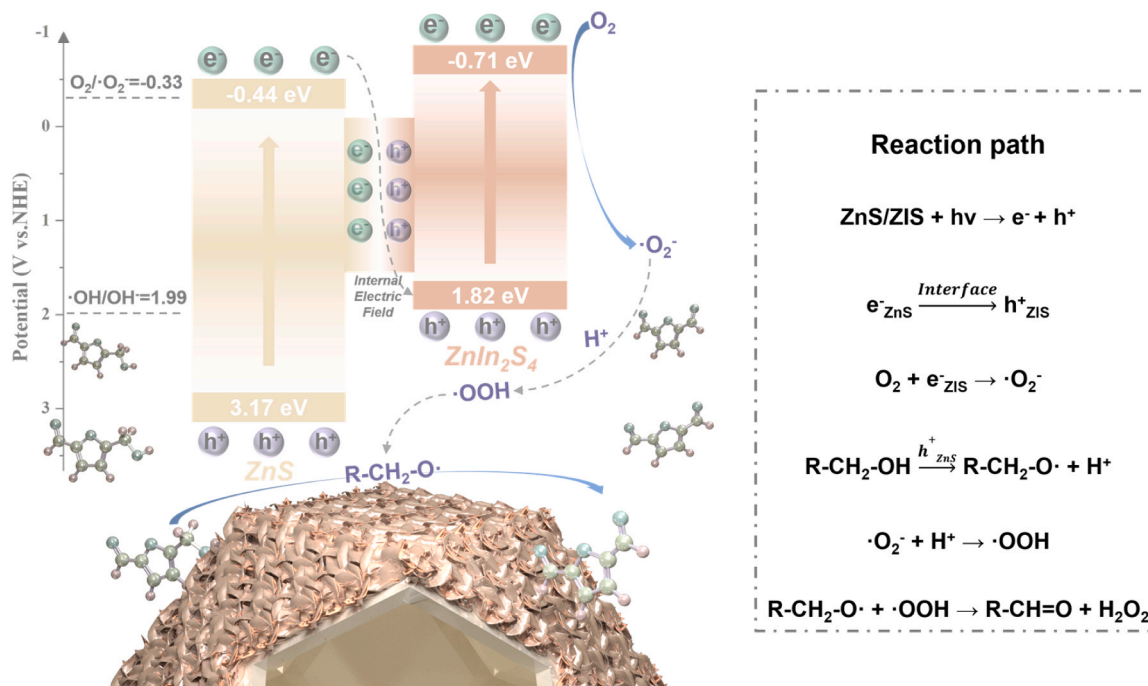


Fig. 11. Derivation of a reaction pathway from HMF to DFF for ZnS/ZIS photocatalysis.

the environment to produce the main reactive radical of the reaction,  $\cdot\text{O}_2^-$ . The hole of ZnS plays a dominant role in the selective conversion of HMF to an alcoholate anion intermediate by dehydrogenation, and  $\cdot\text{O}_2^-$  combines with the removed  $\text{H}^+$  to yield  $\cdot\text{OOH}$ , which further oxidises the substrate to DFF. The holes on the ZnS inside the hollow nanoreactor and the electrons on the external ZIS nanosheets are spatially separated, and the electron-hole composite pathway is blocked, thus providing a greater possibility for the reaction to occur. Fig. 11 illustrates the reaction path of the ZnS/ZIS heterostructure for the oxidation of HMF to DFF under visible light.

#### 4. Conclusion

To summarize, in this paper, ZnS and ZIS were composited together to constitute an S-scheme heterostructure hollow photocatalytic nanoreactor with excellent catalytic properties. Hollow ZnS/ZIS not only has a more regular morphology in three-dimensional space but also gives the material a larger specific surface area in the plane to provide more active and attachment sites. The S-scheme heterojunction formed by the two materials provides a wider range of adaptability in visible light response, photogenerated carrier migration, and photocurrent density for catalysis, which all contribute to the performance enhancement of catalytic HMF. Moreover, the catalyst is applicable to glucose, benzyl alcohol and furfuryl alcohol. During the derivation of the mechanism, the hollow ZnS/ZIS nanoreactor was found to inhibit the electron return and prompt the hole-electron pair separation, which may be due to the specificity of the hollow nanoreactor leading to the obstruction of electron and hole recombination paths, in addition to the role of the S-scheme heterojunction. Through relevant experiments and characterizations, this work fully confirms the reaction mechanism of ZnS/ZIS photocatalytic HMF to DFF, which provides a revelatory role for the construction of heterogeneous nanoreactors based on hollow ZnS structures and the development of more applications. This synthetic strategy is expected to be extended to a series of new ZnS heterojunctions for value-added transformation of biomass-based platform compounds.

#### CRediT authorship contribution statement

**Rui Zhang:** Writing – review & editing. **Xuebin Lu:** Writing – review & editing, Supervision, Resources, Funding acquisition, Conceptualization. **Runyu Liu:** Methodology, Formal analysis. **Yiming Li:** Writing – review & editing, Supervision, Software. **Jian Xiong:** Supervision, Data curation. **Yina Qiao:** Project administration, Formal analysis. **Yuxin Zhang:** Writing – original draft, Data curation, Conceptualization. **Ming Zhang:** Writing – review & editing, Resources, Investigation. **Zhihao Yu:** Writing – review & editing, Visualization.

#### Declaration of Competing Interest

The authors declare no conflict of interest

#### Data availability

The data that has been used is confidential.

#### Acknowledgments

This work was supported by China Postdoctoral Science Foundation (Grant No. 2023M732589), National Natural Science Foundation of China (Grant No. 51908400, 52066017), Central Financial Support Special Funds for Local Universities (Tibet University) ([2022] No. 1, [2023] No. 1, [2024] No. 1), Tibet University Postgraduate High Level Talent Training Programme (Grant No. 2020-GSP-B017), Key R&D Projects in Tibet Autonomous Region (Grant No. XZ202101ZY0011G, XZ202101ZY0012G, XZ202202YD0016C, XZ202202YD0027C).

#### Appendix A. Supporting information

Supplementary data associated with this article can be found in the online version at doi:10.1016/j.apcatb.2024.123914.

#### References

- [1] Y.-W. Han, L. Ye, T.-J. Gong, Y. Fu, Surface-controlled CdS/Ti3C2 MXene schottky junction for highly selective and active photocatalytic dehydrogenation-reductive amination, *Angew. Chem.* 135 (2023) e202306305, <https://doi.org/10.1002/ange.202306305>.
- [2] S.-H. Li, S. Liu, J. Carlos Colmenares, Y.-J. Xu, A sustainable approach for lignin valorization by heterogeneous photocatalysis, *Green Chem.* 18 (2016) 594–607, <https://doi.org/10.1039/C5GC02109J>.
- [3] S.-H. Li, M.-Y. Qi, Z.-R. Tang, Y.-J. Xu, Nanostructured metal phosphides: from controllable synthesis to sustainable catalysis, *Chem. Soc. Rev.* 50 (2021) 7539–7586, <https://doi.org/10.1039/D1CS00323B>.
- [4] F.-K. Shang, Y.-H. Li, M.-Y. Qi, Z.-R. Tang, Y.-J. Xu, Photocatalytic materials for sustainable chemistry via cooperative photoredox catalysis, *Catal. Today* 410 (2023) 85–101, <https://doi.org/10.1016/j.cattod.2022.04.007>.
- [5] M.-Y. Qi, M. Conte, M. Anpo, Z.-R. Tang, Y.-J. Xu, Cooperative coupling of oxidative organic synthesis and hydrogen production over semiconductor-based photocatalysts, *Chem. Rev.* 121 (2021) 13051–13085, <https://doi.org/10.1021/acs.chemrev.1c00197>.
- [6] Y. Lu, T. Liu, C.-L. Dong, Y.-C. Huang, Y. Li, J. Chen, Y. Zou, S. Wang, Tuning the selective adsorption site of biomass on Co3O4 by Ir single atoms for electrosynthesis, *Adv. Mater.* 33 (2021) 2007056, <https://doi.org/10.1002/adma.202007056>.
- [7] M. Kim, Y. Su, A. Fukuoka, E.J.M. Hensen, K. Nakajima, Aerobic oxidation of 5-(Hydroxymethyl)furfural cyclic acetal enables selective furan-2,5-dicarboxylic acid formation with CeO2-supported gold catalyst, *Angew. Chem. Int. Ed.* 57 (2018) 8235–8239, <https://doi.org/10.1002/anie.201805457>.
- [8] M. Zhang, Z. Yu, J. Xiong, R. Zhang, X. Liu, X. Lu, One-Step Hydrothermal synthesis of CdInyS(X+1.5y) for photocatalytic oxidation of biomass-derived 5-hydroxymethylfurfural to 2, 5-diformylfuran under ambient conditions, *Appl. Catal. B Environ.* 300 (2022) 120738, <https://doi.org/10.1016/j.apcatb.2021.120738>.
- [9] Y. Lei, B. Lin, J. Wang, W. Chen, X. Dai, X. Ma, L. Li, Naphthalene-based semiconducting microporous polyimides for high-efficiency photo-catalytic dye degradation, *Polym. Chem.* 14 (2023) 4736–4742, <https://doi.org/10.1039/D3PY00814B>.
- [10] Y.-H. Li, F. Zhang, Y. Chen, J.-Y. Li, Y.-J. Xu, Photoredox-catalyzed biomass intermediate conversion integrated with H2 production over Ti3C2Tx/CdS composites, *Green. Chem.* 22 (2020) 163–169, <https://doi.org/10.1039/C9GC03332G>.
- [11] K. Zhang, L. Guo, Metal sulphide semiconductors for photocatalytic hydrogen production, *Catal. Sci. Technol.* 3 (2013) 1672–1690, <https://doi.org/10.1039/C3CY00018D>.
- [12] H. Wang, L. Zhang, Z. Chen, J. Hu, S. Li, Z. Wang, J. Liu, X. Wang, Semiconductor heterojunction photocatalysts: design, construction, and photocatalytic performances, *Chem. Soc. Rev.* 43 (2014) 5234–5244, <https://doi.org/10.1039/C4CS00126E>.
- [13] P. Wang, X. Zhang, J. Zhang, S. Wan, S. Guo, G. Lu, J. Yao, X. Huang, Precise tuning in platinum-nickel/nickel sulfide interface nanowires for synergistic hydrogen evolution catalysis, *Nat. Commun.* 8 (2017) 14580, <https://doi.org/10.1038/ncomms14580>.
- [14] J. Joo, T. Kim, J. Lee, S.-I. Choi, K. Lee, Morphology-controlled metal sulfides and phosphides for electrochemical water splitting, *Adv. Mater.* 31 (2019) 1806682, <https://doi.org/10.1002/adma.201806682>.
- [15] L. Shen, L. Yu, H.B. Wu, X.-Y. Yu, X. Zhang, X.W. Lou, (David) Formation of Nickel Cobalt Sulfide Ball-in-Ball Hollow Spheres with Enhanced Electrochemical Pseudocapacitive Properties, *Nat. Commun.* 6 (2015) 6694, <https://doi.org/10.1038/ncomms7694>.
- [16] J.-Y. Li, C.-L. Tan, M.-Y. Qi, Z.-R. Tang, Y.-J. Xu, Exposed zinc sites on hybrid ZnIn2S4@CdS nanocages for efficient regioselective photocatalytic epoxide alcoholysis, *Angew. Chem. Int. Ed.* 62 (2023) e202303054, <https://doi.org/10.1002/anie.202303054>.
- [17] R. Zeng, K. Lian, B. Su, L. Lu, J. Lin, D. Tang, S. Lin, X. Wang, Versatile Synthesis of Hollow Metal Sulfides Via Reverse Cation Exchange Reactions for Photocatalytic CO2 reduction, *Angew. Chem. Int. Ed.* 60 (2021) 25055–25062, <https://doi.org/10.1002/anie.202110670>.
- [18] R. Ranjan, A. Chakraborty, R. Ganguly, S. Mukhopadhyay, Employing Cu(II) Complexes of N,O-donor ligand for catalysis in visible light driven cleavage of lignin C-C Bonds, *Mol. Catal.* 537 (2023) 112947, <https://doi.org/10.1016/j.mcat.2023.112947>.
- [19] Y. Chen, Y. Yang, X. Liu, X. Shi, C. Wang, H. Zhong, F. Jin, Sustainable production of formic acid and acetic acid from biomass, *Mol. Catal.* 545 (2023) 113199, <https://doi.org/10.1016/j.mcat.2023.113199>.
- [20] M. Zhang, Z. Li, X. Xin, J. Zhang, Y. Feng, H. Lv, Selective valorization of 5-hydroxymethylfurfural to 2,5-diformylfuran using atmospheric O2 and MAPbBr3 perovskite under visible light, *ACS Catal.* 10 (2020) 14793–14800, <https://doi.org/10.1021/acscatal.0c04330>.
- [21] J. Yang, X. He, J. Dai, R. Tian, D. Yuan, Photo-assisted enhancement performance for rapid detoxification of chemical warfare agent simulants over versatile



- ZnIn<sub>2</sub>S<sub>4</sub>/UiO-66-NH<sub>2</sub> nanocomposite catalysts, *J. Hazard. Mater.* 417 (2021) 126056, <https://doi.org/10.1016/j.jhazmat.2021.126056>.
- [22] P. Zhang, B.Y. Guan, L. Yu, X.W. (David) Lou, Facile synthesis of multi-shelled ZnS-CdS Cages with enhanced photoelectrochemical performance for solar energy conversion, *Chem* 4 (2018) 162–173, <https://doi.org/10.1016/j.chempr.2017.10.018>.
- [23] D. Aouf, A. Henni, D. Selloum, Y. Khane, F. Fenniche, D. Zerrouki, H. Belkhalifa, N. Dizge, Facile preparation and characterization of nanostructured ZnS/PbS heterojunction thin films for enhanced microbial inhibition and photocatalytic degradation, *Mater. Chem. Phys.* 295 (2023) 127059, <https://doi.org/10.1016/j.matchemphys.2022.127059>.
- [24] X. Cao, Z. Chen, R. Lin, W.-C. Cheong, S. Liu, J. Zhang, Q. Peng, C. Chen, T. Han, X. Tong, Y. Wang, R. Shen, W. Zhu, D. Wang, Y. Li, A Photochromic composite with enhanced carrier separation for the photocatalytic activation of benzylic C-H bonds in toluene, *Nat. Catal.* 1 (2018) 704–710, <https://doi.org/10.1038/s41929-018-0128-z>.
- [25] M. Zhang, Y. Zhang, L. Ye, Z. Yu, R. Liu, Y. Qiao, L. Sun, J. Cui, X. Lu, In situ fabrication Ti<sub>3</sub>C<sub>2</sub>F<sub>x</sub> MXene/CdIn<sub>2</sub>S<sub>4</sub> schottky junction for photocatalytic oxidation of HMF to DFF under visible light, *Appl. Catal. B Environ.* 330 (2023) 122635, <https://doi.org/10.1016/j.apcatb.2023.122635>.
- [26] M. Zhang, Z. Yu, J. Xiong, R. Zhang, X. Liu, X. Lu, One-step hydrothermal synthesis of Cd<sub>x</sub>In<sub>y</sub>S<sub>(X+1.5y)</sub> for photocatalytic oxidation of biomass-derived 5-hydroxymethylfurfural to 2, 5-diformylfuran under ambient conditions, *Appl. Catal. B Environ.* 300 (2022) 120738, <https://doi.org/10.1016/j.apcatb.2021.120738>.
- [27] H. Wang, D. Huang, Q. Zhuge, Y. Wu, Oxygen vacancies mediated enhanced visible-light-driven photocatalytic oxidation of biomass derived 5-hydroxymethylfurfural over V<sub>2</sub>O<sub>5</sub>-nH<sub>2</sub>O/g-C<sub>3</sub>N<sub>4</sub> composite, *Diam. Relat. Mater.* 139 (2023) 110413, <https://doi.org/10.1016/j.diamond.2023.110413>.
- [28] J. Xue, C. Huang, Y. Zong, J. Gu, M. Wang, S. Ma, Fe (III)-Grafted Bi<sub>2</sub>MoO<sub>6</sub> nanoplates for enhanced photocatalytic activities on tetracycline degradation and HMF oxidation, *Appl. Organomet. Chem.* 33 (2019) e5187, <https://doi.org/10.1002/aoc.5187>.
- [29] C. Ayed, W. Huang, G. Kizilsavas, K. Landfester, K.A.I. Zhang, Photocatalytic partial oxidation of 5-hydroxymethylfurfural (HMF) to 2,5-diformylfuran (DFF) over a covalent triazine framework in water, *ChemPhotoChem* 4 (2020) 571–576, <https://doi.org/10.1002/cptc.202000070>.
- [30] A. Akhundi, E.I. García-López, G. Marci, A. Habibi-Yangjeh, L. Palmisano, Comparison between preparative methodologies of nanostructured carbon nitride and their use as selective photocatalysts in water suspension, *Res. Chem. Intermed.* 43 (2017) 5153–5168, <https://doi.org/10.1007/s11164-017-3046-9>.
- [31] A. Pan, X. Ma, S. Huang, Y. Wu, M. Jia, Y. Shi, Y. Liu, P. Wangyang, L. He, Y. Liu, CsPbBr<sub>3</sub> Perovskite nanocrystal grown on MXene Nanosheets for enhanced photoelectric detection and photocatalytic CO<sub>2</sub> reduction, *J. Phys. Chem. Lett.* 10 (2019) 6590–6597, <https://doi.org/10.1021/acs.jpclett.9b02605>.
- [32] X. Peng, L. Ye, Y. Ding, L. Yi, C. Zhang, Z. Wen, Nanohybrid photocatalysts with ZnIn<sub>2</sub>S<sub>4</sub> nanosheets Encapsulated UiO-66 octahedral nanoparticles for visible-light-driven hydrogen generation, *Appl. Catal. B Environ.* 260 (2020) 118152, <https://doi.org/10.1016/j.apcatb.2019.118152>.
- [33] M. Dai, Z. He, W. Cao, J. Zhang, W. Chen, Q. Jin, W. Que, S. Wang, Rational construction of S-scheme BN/MXene/ZnIn<sub>2</sub>S<sub>4</sub> heterojunction with interface engineering for efficient photocatalytic hydrogen production and chlorophenols degradation, *Sep. Purif. Technol.* 309 (2023) 123004, <https://doi.org/10.1016/j.seppur.2022.123004>.
- [34] Y.-J. Yuan, P. Wang, Z. Li, Y. Wu, W. Bai, Y. Su, J. Guan, S. Wu, J. Zhong, Z.-T. Yu, Z. Zou, The role of bandgap and interface in enhancing photocatalytic H<sub>2</sub> generation activity of <sup>2</sup>D-<sup>2</sup>D black phosphorus/MoS<sub>2</sub> photocatalyst, *Appl. Catal. B Environ.* 242 (2019) 1–8, <https://doi.org/10.1016/j.apcatb.2018.09.100>.
- [35] Z. Zhang, J.T. Yates, Band bending in semiconductors: chemical and physical consequences at surfaces and interfaces, *Chem. Rev.* 112 (2012) 5520–5551, <https://doi.org/10.1021/cr3000626>.
- [36] M. Zhang, Z. Yu, Y. Zhang, L. Sun, J. Cui, J. Xiong, Y. Han, X. Lu, Photocatalytic conversion of 5-hydroxymethylfurfural to 2,5-diformylfuran by s-scheme black phosphorus/CdIn<sub>2</sub>S<sub>4</sub> heterojunction, *Catal. Sci. Technol.* 13 (2023) 6640–6652, <https://doi.org/10.1039/D3CY01075A>.
- [37] F. Liu, C.-X. Xiao, L.-H. Meng, L. Chen, Q. Zhang, J.-B. Liu, S. Shen, J.-K. Guo, C.-T. Au, S.-F. Yin, Facile fabrication of octahedral CdS-ZnS by cation exchange for photocatalytic toluene selective oxidation, *ACS Sustain. Chem. Eng.* 8 (2020) 1302–1310, <https://doi.org/10.1021/acssuschemeng.9b06802>.
- [38] Y. Li, S. Ouyang, H. Xu, X. Wang, Y. Bi, Y. Zhang, J. Ye, Constructing solid-gas-interfacial fenton reaction over alkalized-C<sub>3</sub>N<sub>4</sub> photocatalyst to achieve apparent quantum yield of 49 % at 420 Nm, *J. Am. Chem. Soc.* 138 (2016) 13289–13297, <https://doi.org/10.1021/jacs.6b07272>.
- [39] Y. Guo, B. Liu, J. Zhang, G. Wang, C. Pan, H. Zhao, C. Wang, F. Yu, Y. Dong, Y. Zhu, Perylene imide supermolecule promote oxygen to superoxide radical for ultrafast photo-oxidation of 5-hydroxymethylfurfural, *Appl. Catal. B Environ.* 340 (2024) 123217, <https://doi.org/10.1016/j.apcatb.2023.123217>.